Asymmetric excitations of toroidal dipole resonance and magnetic dipole quasi-bound state in the continuum in hybrid graphene-dielectric metasurface

Zhiqiang Hao,* Yune Gao, and Cuiying Song
Tianjin University of Commerce, School of Science, Department of Physics, Tianjin, China

Abstract. We study asymmetric excitations of toroidal dipole resonance and magnetic dipole quasi-bound state in the continuum (BIC) in hybrid graphene-dielectric metasurface consisting of a nanoring and a *Y*-shaped nanobar. Through reducing or increasing inner radius of nanoring, the quasi-BIC dominated by magnetic dipole moment can be excited and effectively modulated via adjusting the Fermi energy and layer numbers of the graphene. The proposed metasurface can not only produce a symmetric localized magnetic field distribution but also create two asymmetric localized magnetic field distributions in near-infrared wavelength, providing a new way of indirectly manipulating the localized magnetic field enhancement. Our results can be of practical interest for a variety of applications including optical modulator, filter, switches and light trapping. © *2022 Society of Photo-Optical Instrumentation Engineers (SPIE)* [DOI: 10.1117/1.JNP.16.046003]

Keywords: dielectric metasurfaces; quasi-bound states in the continuum; graphene; tenability.

Paper 22052G received Jun. 10, 2022; accepted for publication Oct. 26, 2022; published online Nov. 10, 2022.

1 Introduction

Dielectric resonator-based Fano resonances in metasurfaces have been given much attention in recent years for the unique properties to greatly improve the performance of enhanced spectroscopy,[1,2] biosensing,[3–5] and nonlinear effect.[6–8] Fano resonances in such metasurfaces represent a universal wave interference phenomenon manifested as a distinct asymmetric spectral line shape due to coherent coupling between a discrete state and a continuous state. Such interference gives rise to Fano resonance phenomenon in a dielectric metasurface, also restricts the independent tunability of the individual resonances without any mutual influence due to the collective behavior of the total resonant systems. Recently, several all-dielectric structures have been applied to generate dominant toroidal dipole (TD) Fano resonances[9,10] by symmetry breaking to acquire high Q-factors. The TD Fano resonances excited in symmetry-breaking structures mainly depend on altering the geometry. However, the asymmetric magnetic field enhancements and Q-factors of TD Fano resonances in the existing work are still insufficient, which require further explorations in structure design and physical mechanism innovation. And, independent tailoring magnetic field is already one of the challenges to meet the demands in the targeted functionalities, but few research works have focused on that.

Recently, Fano resonance has also been linked to bound states in continuum (BIC), which can produce extremely high Q-factor resonances and appears first in quantum mechanics. A true BIC only appears in ideal lossless infinite structures or extreme values of parameters, its resonance linewidth disappears and manifests itself as a collapse of Fano resonance while its Q-factor is infinite.[11–16] In practice, symmetry-protected BIC can be transformed into quasi-BIC with a finite yet sharply high Q resonance by breaking the symmetry. And such peculiar quasi-BIC state has also been reported in subwavelength-resonant particles,[17,18] metasurfaces,[19–22] coupled waveguide arrays,[23–25] and photonic crystal cavities.[26–28] And the quasi-BIC has been demonstrated outstanding performances in various applications, especially for laser[29,30] and nonlinear.[31–34] However, the existence of quasi-BIC strongly depends on the geometrical

*Address all correspondence to Zhiqiang Hao, hzq798@126.com

parameters, and it is difficult to realize asymmetric excitation for quasi-BIC resulting from the collective effect in Fano resonance.

In this paper, we theoretically demonstrate that the hybrid graphene-dielectric metasurface consisting of a nanoring and a *Y*-shaped nanobar can support simultaneously asymmetric excitations of TD Fano resonance and MD quasi-BIC. Through reducing or increasing inner radius of nanoring, the quasi-BIC dominated by MD moment can be excited and effectively modulated by Fermi energy and layer numbers of the graphene. We explain the physical mechanism of quasi-BIC state in terms of the near-field enhancement and multipole decomposition, and such state is further confirmed by the quadratic inverse trend between the Q-factor and asymmetry parameter. Furthermore, the proposed metasurface can not only produce a symmetric localized magnetic field distribution but also create two asymmetric localized magnetic field distributions in near-infrared wavelength, providing a new way of indirectly manipulating the localized magnetic field enhancement.

2 Numerical Methods

The schematic diagram of the proposed hybrid graphene-dielectric metasurface is shown in Fig. 1. Each unit cell consists of graphene overlayer lying on the amorphous silicon (Si) metasurface with the silica (SiO_2) substrate. The dielectric metasurface without graphene layer is composed of a nanoring and Y-shaped nanobar, as given in Fig. 1(b), the nanoring has the same outer radius R and different inner radius R_1 and R_2, the Y-shaped nanobar has the same width W. Numerical simulations are conducted using the finite difference time domain and finite element method, where periodic boundary conditions are applied along both the x- and y- directions, and the normal beam propagation direction ($-z$ axis) is bounded with 32 perfectly matched layers. The dielectric constants of Si and SiO_2 can be referred from the Palik handbook.[35] Surface conductivity of graphene can be well derived with the random-phase approximation theory.[36] Linearly polarized wave is normal incidence and the polarization angle θ is measured from y-axis, as shown in Fig. 1(b).

3 Simulation Results and Discussions

Figure 2(a) shows the transmission spectrum of the proposed metasurface without the graphene overlayer at the $\theta = 0$ deg. The structure parameters are $R = 400$ nm, and $R_1 = R_2 = 280$ nm, $W = 120$ nm, $T = 140$ nm and $Px = Py = 900$ nm. One can clearly observe a sharp Fano resonance dip at 1378 nm with the spectral contrast ratio near 100%, defined as $[(T\text{peak} - T\text{dip})]/[(T\text{peak} + T\text{dip})] \times 100\%$. Figure 2(b) shows three dominant Cartesian multipole moments based on the density of displacement currents $J(r) = -i\omega\varepsilon_0(n_2 - 1)E(r)$.[15] The transmission curve can obtain a relatively high Q-factor owing to the low radiated loss reduced by the enhanced TD Ty and suppressed electric dipole Py and magnetic dipole Mx, as shown in Fig. 2(b). And the radiating intensity of the TD is 11 times bigger than that of the ED. In addition,

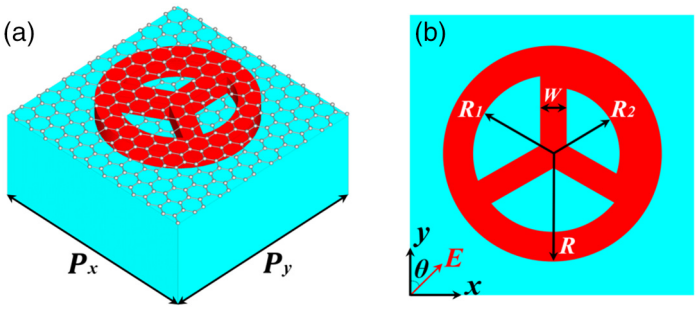

Fig. 1 (a) Schematic diagram of a unit cell in the proposed hybrid graphene-dielectric metasurface. (b) Top view of the unit cell without graphene layer. Geometric parameters are denoted in Fig. 1.

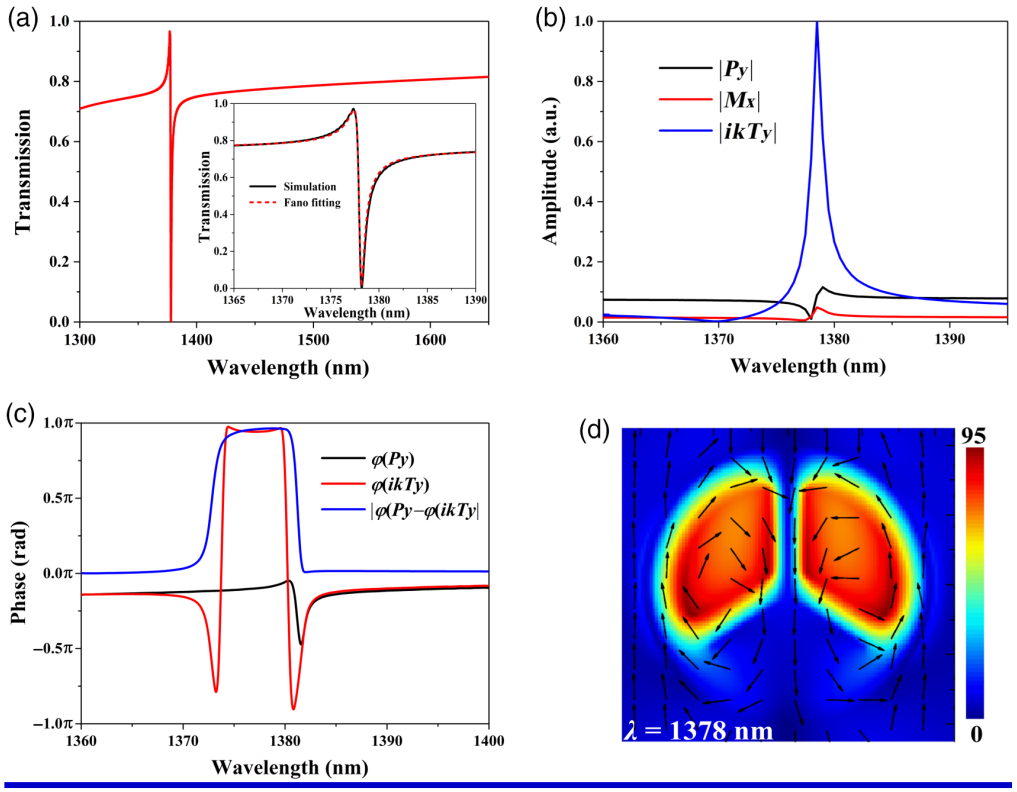

Fig. 2 (a) Transmission spectrum of all-dielectric metasurface without a graphene overlayer at $\theta = 0$ deg. Inset represents the fitted spectrum near the resonance. (b) Normalized power scattered by different multipoles, including Cartesian TD $|ikTy|$, electric dipole $|Py|$, and magnetic dipole $|Mx|$ moment around 1378 nm at $\theta = 0$ deg. (c) The phases and their difference of $\varphi(Py)$ and $\varphi(ikTy)$. (d) Simulated distributions of magnetic field enhancement ($|H/H_0|$) in the xy plane at a resonant wavelength of 1378 nm.

the phase difference $|\varphi(Py) - \varphi(ikTy)|$ is approximately equal to π around 1378 nm, as shown in Fig. 2(c), where the destructive interference of the far-field radiation between the ED and TD resonances produces the asymmetric TD Fano resonance at 1378 nm. Magnetic field enhancement ($|H/H0|$) in the xy plane can be firmly constrained within the two symmetric holes along the y axis by the enhanced Ty and no radiation energy transmits outward at 1378 nm, as shown in Fig. 2(d). And the maximum magnetic field enhancement at 1378 nm reaches 95. The inset in Fig. 2(a) analyzes the transmission spectrum of the metasurface and proves rigorously that it can be described by the classical Fano formula:

$$T_{\text{Fano}} = \left| a_1 + ia_2 + \frac{b}{\omega - \omega_0 + i\gamma} \right|^2,$$

where a_1, a_2 and b are constants; ω is the central oscillation frequency; and γ is the leakage rate.[37] The analytical derivation can reproduce exactly Fano resonance attained from simulation at $\theta = 0$ deg. And the corresponding Q-factor can be calculated with the $\omega_0/2$ and reaches 4521.

Figure 3(a) shows the evolution of transmission spectra of the metasurface without the graphene overlayer as a function of the R_2. In addition to the TD Fano resonance near 1375 nm, the detailed transmission spectra shown in Fig. 3(a) exhibit a narrow dip at longer wavelength that entirely vanishes around 1515 nm when the unit cell becomes symmetric ($R_1 = R_2 = 280$ nm). We observe that BIC with infinite Q-factor transforms into high-Q quasi-BIC whose radiation loss grows with the modulated R_2. In Figs. 3(b) and 3(c), we decompose the far-field radiation of Fano resonance and quasi-BIC into contributions of different multipole components under the Cartesian coordinate. As shown in Fig. 2(b), the normalized power scattered by the Cartesian

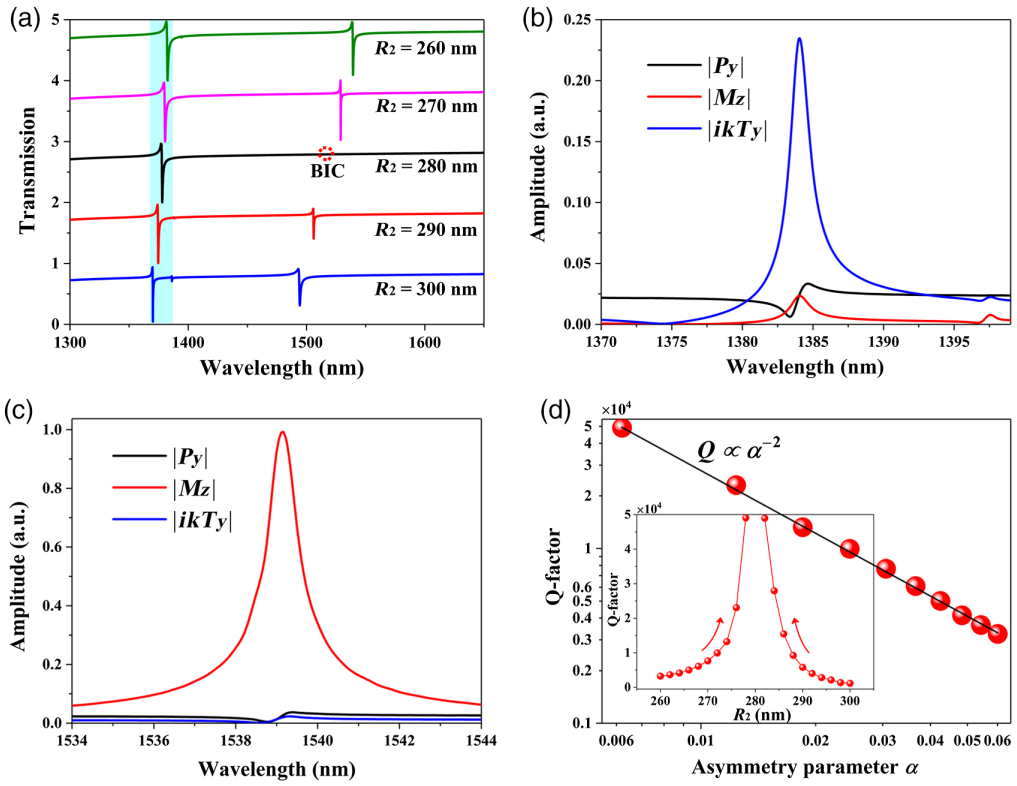

Fig. 3 (a) Evolution of transmission spectra of the metasurface without graphene overlayer as a function of the R_2. Other parameters are the same as that used in Fig. 2(a). (b) and (c) Normalized power scattered by the Cartesian TD moment $|ikTy|$, ED moment $|Py|$, and MD moment $|Mz|$ around 1383 and 1539 nm when $R_2 = 260$ nm. (d) Log–log plot of radiative Q factors as a function of the asymmetric degree $\alpha = \Delta S/S$ for $R_2 > 280$-nm case. The black line shows the inverse quadratic dependence of $\Delta S/S$. Inset represents the extracted Q-factors of the quasi-BIC versus the radius R_2.

TD moment dominates Fano resonance around 1383 nm. After introduction of the symmetry perturbation ($R_1 \neq R_2$), the MD component possessing radiation along the z axis emerges in Fig. 3(c), resulting in the excitation of quasi-BIC. Such dominant MD also manifests itself in the near-field distribution in Figs. 4. As shown in Fig. 3(d), the evolution of the Q-factors on the asymmetry parameter ($\alpha = \Delta S/S$) was dominated by the inverse quadratic law

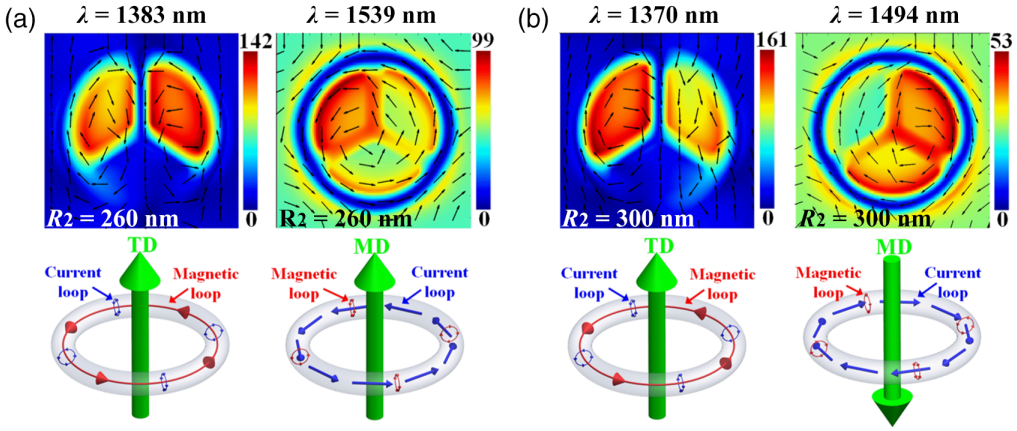

Fig. 4 Distributions of the enhanced magnetic field ($|H|/|H0|$) and schematics of the formation of the corresponding TD and quasi-BIC modes in metasurface (a) $R_2 = 260$ nm and (b) $R_2 = 300$ nm, respectively. The black arrows show the electric field directions.

$Q_{\text{rad}} = Q_0\alpha^{-2}$, where Q_0 is a constant determined by the design of structure. Note that for the larger asymmetry parameter α the Q-factor is significantly reduced because the large deviation from the symmetric unit cell cannot be treated as a tiny perturbation. As the linewidth of the quasi-BIC disappears, its Q-factor diverges, as shown in the inset in Fig. 3(d), which further manifests the formation of a BIC. At the BIC points ($R_1 = R_2 = 280$ nm), the radiative Q-factor diverges, which causes the total Q-factor to be limited by the loss in the system. Therefore, the total Q-factor of the symmetry-protected BIC will diverge to infinity due to the absence of loss.

Figure 4 shows the normalized magnetic field enhancement and electric field directions in the xy plane. The electric field directions in the xy plane forms two reversed current loops at $\lambda = 1383$ nm and $\lambda = 1370$ nm, where the anti-phase oscillations of current loops lead to the suppression of the ED and MD, and the spatially localized magnetic field in the xz plane forms a loop, confirming the in-plane TD response. While the electric field directions in the xy plane forms a swirl at $\lambda = 1539$ nm and $\lambda = 1494$ nm, indicating a typical z-orientated MD feature. And the corresponding TD and MD can be further confirmed by corresponding artistic illustrations in Fig. 4. It is worth mentioning that asymmetric magnetic hotspot of TD Fano resonances at 1383 and 1370 nm is always localized in the smaller two holes, while the asymmetric magnetic hotspot of the quasi-BIC resonances at 1492 and 1550 nm is always localized in the bigger holes, whether the R_2 is greater than or <280 nm. In addition, thanks to the high Q-factors of TD Fano resonance, the maximum magnetic field can be enhanced by more than 160 times at $\lambda = 1370$ nm, comparable to plasmonic nanostructures.

Figure 5(a) shows the calculated transmission spectra as a function of the wavelength with the incident angle from $\varphi = 0$ deg to 10 deg. It is clearly shown that the resonance at 1378 nm becomes sharper and finally vanishes, while a new resonant mode grows wider in the wavelength range of 1500 to 1600 nm as the φ increases. This sharp resonant features indicate the existence of BIC mode in the structure. Such sharp resonance, which can be analyzed more clearly from the multipole analysis shown in Fig. 5(b). This dominant magnetic dipole resonance manifest itself in the near-field distribution in the xy plane in the inset. We can see that the electric field in the xy plane forms a loop, which means the linearly polarized magnetic field along the z axis in the xy plane, corresponding to an MD resonance mode. Due to the weak resonance strength, the new resonance with $\varphi = 4$ deg at 1395 nm will not be discussed here.

Graphene has attracted enormous interest due to its unique electronic and optical properties.[38] Numerous graphene-based metasurface/metamaterials have been investigated over the past few years.[36,39] To further investigate the influence of the Fermi energy (E_F) and layer numbers of graphene on the quasi-BIC, we study transmission spectra of the hybrid graphene-dielectric metasurface. Figure 6(a) shows actively modulated quasi-BIC and TD resonances in the hybrid

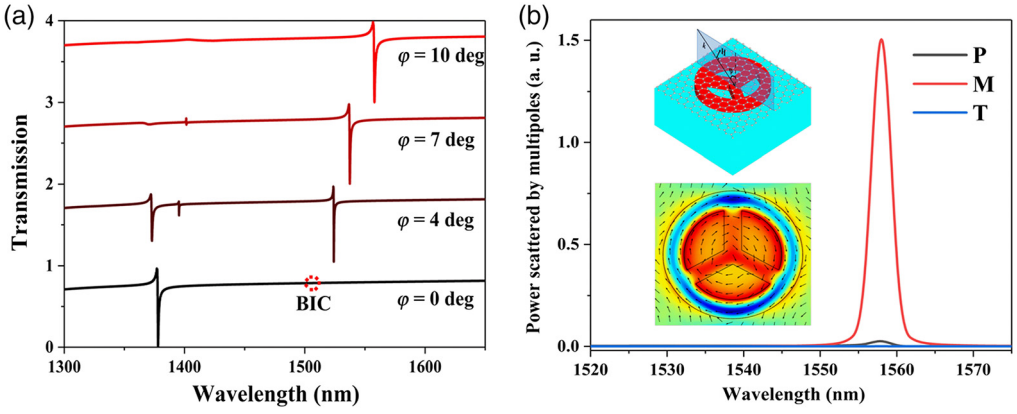

Fig. 5 (a) Transmission spectra with different incident angles φ at $\theta = 0$ deg. (b) Multipolar decomposition of the contributing three multipole moments around 1558 nm at $\varphi = 10$ deg. The insets show the incident angles φ and the enhanced magnetic field ($|H|/|H0|$) at 1558 nm. The black arrows show the electric field directions. Other parameters are the same as that used in Fig. 2(a).

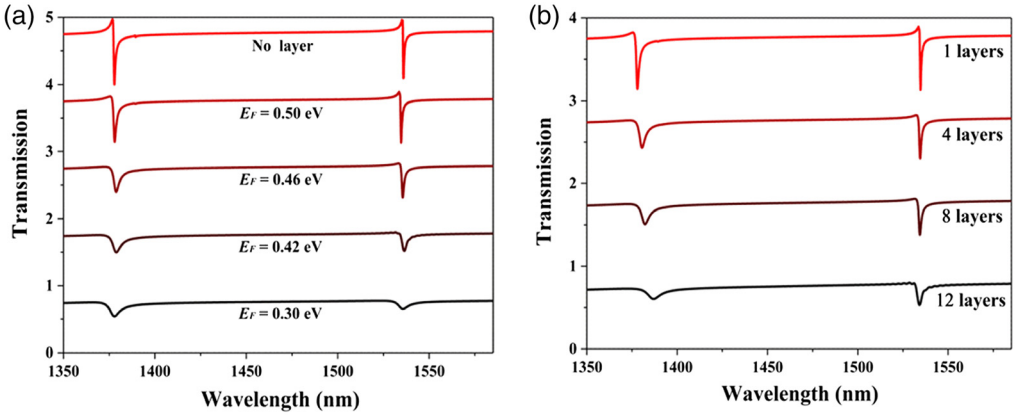

Fig. 6 Simulated transmission spectra at (a) different Fermi level and (b) different layer numbers, showing the active modulation of toroidal dipolar resonance. Other parameters are the same as that used in Fig. 2(a).

graphene-dielectric metasurface only by tuning the E_F of graphene. Such two resonances in hybrid metasurface can be modulated by the introduced graphene and is broadened and almost wiped out with the decrease of the E_F due to the wavelength dependent graphene conductivity for different E_F,[40,41] which results in the rapidly decreased the Q-factors and spectral contrast ratio. To quantify the modulation of the transmission amplitude with the graphene, the modulation in transmittance is defined as $\Delta T = |T_g(E_F = 0.3\ \text{eV}) - T(\text{no layer})| \times 100\%$, where T_g and T represent the transmission amplitude at resonance dip with and without the graphene, respectively. And the largest ΔT modulated for the TD Fano resonance and quasi-BIC can be calculated as high as 66.2% and 78%, respectively. Figure 6(b) shows the transmission spectra versus the wavelength for different layer numbers of graphene. One can see that the quasi-BIC and TD resonances continuously decrease in the resonant intensity as the graphene layer number increases from 1 to 12. In the numerical modeling, the layer number of graphene is set to 1, 4, 8, and 12 with the Fermi energy fixed as $E_F = 0.5$ eV. And the maximum ΔT for the TD Fano resonance and quasi-BIC, defined as $\Delta T = |T_g(12\,\text{layers}) - T_g(1\,\text{layer})| \times 100\%$, reaches 74% and 64%, respectively. It also demonstrates that the proposed hybrid graphene-dielectric metasurface can be effectively modulated by Fermi energy and layer numbers of the graphene, showing a potential application in the active quasi-BIC-based optical modulator.

4 Conclusions

In summary, we have theoretically demonstrated that the hybrid graphene-dielectric metasurface consisting of a *Y*-shaped nanobar and a nanoring is capable of supporting asymmetric excitations of TD resonance and magnetic dipole quasi-bound state in the continuum simultaneously. Through reducing or increasing inner radius of nanoring, the quasi-BIC dominated by magnetic dipole moment can be excited and modulated by altering the the Fermi energy and layer numbers of the graphene and the maximum transmission differences for the quais-BIC and TD resonance reaches 74% and 78%, respectively. In addition, the proposed metasurface can not only produce a symmetric localized magnetic field distribution but also create two asymmetric localized magnetic field distributions in near-infrared wavelength, showing a variety of applications including optical modulator, filter, switches, and light trapping.

Acknowledgments

This work was supported by National Natural Science Foundation of China (Grant No. 11804251).

References

1. A. S. Shorokhov et al., "Multifold enhancement of third-harmonic generation in dielectric nanoparticles driven by magnetic Fano resonances," *Nano Lett.* **16**(8), 4857–4861 (2016).
2. G. Grinblat, "Nonlinear dielectric nanoantennas and metasurfaces: frequency conversion and wavefront control," *ACS Photonics* **8**(12), 3406–3432 (2021).
3. P. P. Vabishchevich et al., "Enhanced second-harmonic generation using broken symmetry III–V semiconductor Fano metasurfaces," *ACS Photonics* **5**(5), 1685–1690 (2018).
4. S. Liu et al., "Resonantly enhanced second-harmonic generation using III−V semiconductor all-dielectric metasurfaces," *Nano Lett.* **16**(9), 5426–5432 (2016).
5. S. Campione et al., "Broken symmetry dielectric resonators for high quality-factor Fano metasurfaces," *ACS Photonics* **3**(12), 2362–2367 (2016).
6. L. T. Ming et al., "Dielectric metasurfaces enabling advanced optical biosensors," *ACS Photonics* **8**(1), 47–60 (2020).
7. W. D. Wang, L. Zheng, and J. G. Qi, "High Q-factor multiple Fano resonances for high-sensitivity sensing in all-dielectric nanocylinder dimer metamaterials," *Appl. Phys. Express* **12**(7), 75002 (2019).
8. Y. Yang et al., "Nonlinear Fano-resonant dielectric metasurfaces," *Nano Lett.* **15**(11), 7388–7393 (2015).
9. M. F. Limonov et al., "Fano resonances in photonics," *Nat. Photonics* **11**, 543–554 (2017).
10. C. Zhou et al., "Optical radiation manipulation of Si-$Ge_2Sb_2Te_5$ hybrid metasurfaces," *Opt. Express* **28**, 9690–9701 (2020).
11. A. A. Bogdanov, M. F. Limonov, and Y. S. Kivshar, "High-Q supercavity modes in subwavelength dielectric resonators," *Phys. Rev. Lett.* **119**(24), 243901 (2017).
12. A. A. Bogdanov et al., "Bound states in the continuum and Fano resonances in the strong mode coupling regime," *Adv. Photonics* **1**(1), 016001 (2019).
13. M. Odit et al., "Observation of supercavity modes in subwavelength dielectric resonators," *Adv. Mater.* **33**(1), 2003804 (2021).
14. S. Han et al., "All-dielectric active terahertz photonics driven by bound states in the continuum," *Adv. Mater.* **31**(37), 1901921 (2019).
15. Y. He et al., "Toroidal dipole bound states in the continuum," *Phys. Rev. B* **98**(16), 161112(R) (2018).
16. E. Melik-Gaykazyan et al., "From Fano to quasi-BIC resonances in individual dielectric nanoantennas," *Nano Lett.* **21**(4), 1765–1771 (2021).
17. D. R. Abujetas et al., "High-Q transparency band in all-dielectric metasurfaces induced by a quasi bound state in the continuum," *Laser Photonics Rev.* **15**(1), 2000263 (2021).
18. A. S. Kupriianov et al., "Metasurface engineering through bound states in the continuum," *Phys. Rev. Appl.* **12**(1), 014024 (2019).
19. M. V. Rybin et al., "High-Q supercavity modes in subwavelerigth dielectric resonators," *Phys. Rev. Lett.* **119**(24), 243901 (2017).
20. J. Gomis-Bresco, D. Artigas, and L. Torner, "Anisotropy-induced photonic bound states in the continuum," *Nat. Photonics* **11**(4), 232–236 (2017).
21. K. Koshelev et al., "Asymmetric metasurfaces with high- Q resonances governed by bound states in the continuum," *Phys. Rev. Lett.* **121**(19), 193903 (2018).
22. M. Liu and D. Y. Choi, "Extreme huygens' metasurfaces based on quasi-bound states in the continuum," *Nano Lett.* **18**(12), 8062–8069 (2018).
23. E. N. Bulgakov and A. F. Sadreev, "Bound states in the continuum in photonic waveguides inspired by defects," *Phys. Rev. B* **78**(7), 075105 (2008).
24. C. W. Hsu et al., "Observation of trapped light within the radiation continuum," *Nature* **499**, 188–191 (2013).
25. M. Rybin and Y. Kivshar, "Supercavity lasing," *Nature* **541**, 164–165 (2017).
26. Y. Plotnik et al., "Experimental observation of optical bound states in the continuum," *Phys. Rev. Lett.* **107**(18), 183901 (2011).
27. M. I. Molina, A. E. Miroshnichenko, and Y. S. Kivshar, "Surface bound states in the continuum," *Phys. Rev. Lett.* **108**(7), 070401 (2012).
28. G. Corrielli et al., "Observation of surface states with algebraic localization," *Phys. Rev. Lett.* **111**(22), 220403 (2013).

29. A. Kodigala et al., "Lasing action from photonic bound states in continuum," *Nature* **541**, 196–199 (2017).
30. M. Wu et al., "Room-temperature lasing in colloidal nanoplatelets via mie-resonant bound states in the continuum," *Nano Lett.* **20**(8), 6005–6011 (2020).
31. A. P. Anthur et al., "Continuous wave second harmonic generation enabled by quasi-bound-states in the continuum on gallium phosphide metasurfaces," *Nano Lett.* **20**(12), 8745–8751 (2020).
32. L. Carletti et al., "High-harmonic generation at the nanoscale boosted by bound states in the continuum," *Phys. Rev. Res.* **1**(2), 023016 (2019).
33. L. Carletti et al., "Giant nonlinear response at the nanoscale driven by bound states in the continuum," *Phys. Rev. Lett.* **121**(3), 033903 (2018).
34. K. Koshelev et al., "Nonlinear metasurfaces governed by bound states in the continuum," *ACS Photonics* **6**(7), 1639–1644 (2019).
35. E. D. Palik, *Handbook of Optical Constants of Solids*, Academic Press, Washington (1985).
36. G. D. Liu et al., "Toroidal resonance based optical modulator employing hybrid graphene-dielectric metasurface," *Opt. Express* **25**(21), 26045 (2017).
37. Y. Yang et al., "All-dielectric metasurface analogue of electromagnetically induced transparency," *Nat. Commun.* **5**(1), 5753 (2014).
38. S. AbdollahRamezani et al., "Analog computing using graphene-based metalines," *Opt. Lett.* **40**(22), 5239–5242 (2015).
39. S. AbdollahRamezani et al., "Beam manipulating by gate-tunable graphene-based meta-surfaces," *Opt. Lett.* **40**(22), 5383–5386 (2015).
40. X. Wang et al., "Controlling light absorption of graphene at critical coupling through magnetic dipole quasi-BIC resonance," *Phys. Rev. B* **102**(15), 155432 (2020).
41. W. Wang et al., "Symmetry-protected bound state in the continuum in the metasurface of dielectric nanodisk with the inclined surface," *J. Mod. Opt.* **68**(13), 699–706 (2021).

Biographies of the authors are not available.